ACS Sustainable Chemistry & Engineering

pubs.acs.org/journal/ascecg

Research Article

Effect of Salinity on CO_2 Thermodiffusion in Aqueous Mixtures by Molecular Dynamics Simulations

Felipe Mourao Coelho, Luis Fernando Mercier Franco, and Abbas Firoozabadi*

Cite This: *ACS Sustainable Chem. Eng.* 2023, 11, 17086−17097

Read Online

ACCESS | Metrics & More | Article Recommendations | Supporting Information

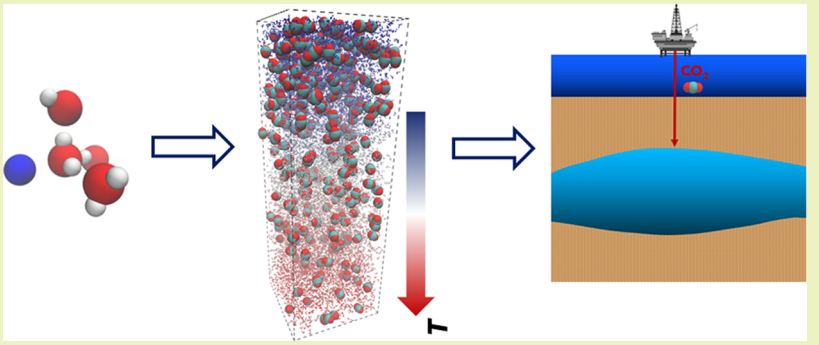

ABSTRACT: Some geothermal formations may contain a large concentration of CO_2 and a very high vertical temperature gradient. It is likely that there may be significant variation in the CO_2 concentration in these formations due to the Soret effect. In our work, we evaluate, for the first time, the CO_2 thermodiffusion in brine mixtures via molecular dynamics simulations. In the past, cross-diffusion effects on thermodiffusion have been neglected in the evaluation of thermal diffusion in three or more species despite their significance. In this work, we present a methodology to compute the thermal diffusion factor in multicomponent mixtures by combining equilibrium and nonequilibrium molecular dynamics simulations. As in binary CO_2−H_2O, the CO_2−brine Soret effect may have a pronounced dependency on temperature; by increasing temperature, CO_2 migrates from thermophobic to thermophilic conditions. Water structure may have a dominant effect on CO_2 thermal diffusion. The more organized the hydrogen bond network, the more thermophobic the CO_2; an increase in temperature or salinity may make CO_2 more thermophilic. Our results and formulations advance the knowledge of CO_2 distribution in subsurface formations and set the stage for accurate modeling of formations aimed at carbon sequestration and heat extraction.

KEYWORDS: *thermodiffusion, electrolytes, carbon sequestration, geothermal energy, molecular dynamics, diffusion*

INTRODUCTION

Carbon capture and sequestration (CCS) is a promising process for mitigating anthropogenic carbon dioxide emissions to the atmosphere.[1−3] Among the subsurface geological formations, deep saline aquifers entail one of the most feasible options for long-term CO_2 storage due to abundance, storage capacity, and operation cost.[4,5] The injection and permanency of CO_2 in a saline aquifer is a result of the interaction of a multicomponent and multiphase mixture between species like CO_2, water, salts, and minerals.

Extraction of geothermal energy via enhanced geothermal systems (EGS) may result in CO_2 production. In some geothermal formations, water and rock react at high temperatures (as high as 400 °C[6]); in such formations, the average CO_2 concentration can be about 7% weight fraction.[7] Knowledge of the distribution of CO_2 inside the formation may lead to more efficient heat extraction. The produced CO_2 can be used as the working fluid in geothermal systems, which has drawn attention by combining both carbon sequestration and energy harvesting.[8,9] The development of CCS and EGS technologies depends on the understanding of the behavior and thermophysical properties of the CO_2−brine mixture under geological conditions.

Thermodynamic and transport properties of CO_2−brine mixtures have been investigated in the past.[10,11] The phase behavior of CO_2 in brine is complex and depends on the pressure, temperature, and salinity. Electrolytes decrease the solubility of CO_2 in the aqueous phase due to the salting-out effect;[12] a reduction in the solubility of about 25% is expected for every 10% in mass fraction of salt concentration.[13] The fluid distribution and behavior within porous media are controlled

Received: August 17, 2023
Revised: October 17, 2023
Accepted: October 19, 2023
Published: November 15, 2023

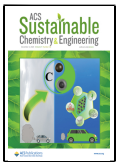

https://doi.org/10.1021/acssuschemeng.3c05269
ACS Sustainable Chem. Eng. 2023, 11, 17086−17097

by wettability and interfacial tension (IFT) between phases.[14] Higher salinity results in higher IFT between the CO_2-rich phase and the aqueous phase due to the cation low affinity for the interface.[14−16] Viscosity and diffusivity determine the flow rate and the migration of CO_2 within the formation.[17] The diffusion coefficient of the dissolved CO_2 decreases with salinity, whereas the viscosity enhances;[18−20] the reduction in CO_2 diffusivity can be as high as 45% for a 4 M NaCl solution.[20] Because geothermal formations have high salinity, understanding the effect of electrolytes on CO_2 properties is essential for CCS and geothermal heat extraction applications.

A temperature gradient may induce a concentration gradient in a mixture. The coupled phenomenon between mass and heat flux is called the Soret effect or thermodiffusion. The physical nature behind the Soret effect remains unclear,[21,22] which makes the prediction and modeling of the phenomenon challenging, especially for associating and multicomponent mixtures. In ideal binary liquids and gases, one expects that the lighter component concentrates in the hot region and the heavier component concentrates in the cold region; this configuration allows more effective heat conduction through the mixture.[23] In hydrocarbon reservoirs, thermodiffusion may overcome gravity segregation depending on the geothermal gradient, leading to an accumulation of the heaviest component on the top of the formation.[24] The geothermal gradient in deep saline aquifers can be higher than 40 $K{\cdot}m^{-1}$,[5] and CO_2 is distributed in the formation due to the Soret effect.

In recent work, we have evaluated the thermodiffusion of the CO_2−H_2O under subsurface conditions.[25] At lower temperatures, CO_2 tends to concentrate in the cold region, where the CO_2−CO_2 interactions are weaker and the hydrogen bonds are more organized. By increasing the temperature, the CO_2 thermodiffusion factor decreases, and a change in the Soret effect direction may occur at 400 K. Thermodiffusion has an opposite trend compared to gravity segregation. At typical subsurface conditions, the Soret effect is more pronounced than gravity segregation, and CO_2 tends to accumulate at the top of the formation (colder region) if there is no salt effect.

The CO_2−brine mixture is a multicomponent system. For a single salt in a solvent, the mixture may be treated as a ternary. Fickian diffusion in a mixture with N components is no longer represented by a single diffusion coefficient but by a $(N-1)\times(N-1)$ nonsymmetrical matrix that could even exhibit negative coefficients.[26] The measurement of the Soret effect in multicomponent mixtures is nontrivial at laboratory conditions, and the available experimental data are limited.[27,28] The cross diffusion between species increases the mixture's susceptibility to perturbations.[28,29] By increasing the number of components in the mixture, classical thermodiffusion model predictions may be inaccurate.[30]

A molecular dynamics (MD) simulation is an alternative to investigating the Soret effect.[23,31−39] Based on force fields, which describe the interaction potentials between species, MD simulations generate molecular trajectories that can be connected to macroscopic properties using statistical mechanics principles. Molecular simulation allows a comprehensive investigation of conditions often inaccessible to experimental investigations, such as high pressure, high temperature, and convection-free mixture. The thermodiffusion of electrolytes in aqueous solution has been studied by MD simulations in the past.[40−44] The Soret effect depends on the solute and the mixture conditions;[40] ion−water interactions play a key role in determining the thermal region where salts concentrate.[42]

In multicomponent mixtures, diffusion by the concentration gradient from other components may affect the thermodiffusion. Artola and Rousseau[45] have investigated the thermodiffusion in a ternary mixture of an isotopic argon mixture by nonequilibrium molecular dynamics (NEMD) simulations. For this ideal mixture, the lighter component accumulates on the hot side and the heavier on the cold side, but the intermediate component behavior depends on the composition and conditions of the mixture. In previous works, the thermal diffusion factor in multicomponent mixtures has been defined as in the binary mixture: only accounting for the thermal segregation of the respective component.[27,30,37,45−47] The validation against experimental data is straightforward in this definition. If the cross-diffusion effect is not accounted for, then the application to thermodiffusion modeling is limited to the exact conditions from where the thermal diffusion factor is computed. To the best of our knowledge, no attempt has been made to compute the thermal diffusion factor of multicomponent mixtures by using MD simulations with consideration of the cross-diffusion effect.

In this work, we evaluate the thermodiffusion of CO_2 in a brine mixture using MD simulations to investigate the impact of salinity. We develop a framework to compute the thermal diffusion factor in multicomponent mixtures combining both equilibrium (EMD) and nonequilibrium molecular dynamics simulations (NEMD). The Fickian and Maxwell−Stefan diffusivities are computed at various conditions as part of a comprehensive formulation. We evaluate the effect of temperature and brine concentration and composition on the CO_2 thermodiffusion. Finally, we investigate the molecular structure at each condition to improve our understanding of the Soret effect.

METHODS

Determination of $\alpha_{T,i}$ in Multicomponent Mixtures. The molar flux J_i of component i in a mixture with N components without viscous flows and with no external forces may be expressed by[48,49]

$$\boldsymbol{J_i} = -c\left(\sum_{j}^{N-1} D_{ij}^{\mathrm{M}}\nabla x_j + x_i x_N D_i^T \nabla T\right) \quad (i = 1, 2 \ldots N-1) \tag{1}$$

where c is the molar density, x_i is the mole fraction of component i, T is the absolute temperature, D_{ij}^{M} is the Fickian diffusion coefficient, and D_i^T is the thermal diffusion coefficient. Thermodiffusion may be quantified by the thermal diffusion factor $\alpha_{T,i}$, which relates to the thermal diffusion coefficient by[50]

$$D_i^T = \frac{\alpha_{T,i} D_{ii}^{\mathrm{M}}}{T} \quad (i = 1, 2 \ldots N-1) \tag{2}$$

By combining eqs 1 and 2, at steady state ($\boldsymbol{J_i} = 0$), we arrive at an expression for the thermal diffusion factor in a multicomponent mixture

$$\alpha_{T,i} = -\frac{T}{x_i x_N}\sum_{j=1}^{N-1}\frac{D_{ij}^{\mathrm{M}}}{D_{ii}^{\mathrm{M}}}\frac{\mathrm{d}x_j}{\mathrm{d}T} \quad (i = 1, 2 \ldots N-1) \tag{3}$$

In the literature, the thermal diffusion factor is expressed as $\alpha'_{T,i} = -[T/(x_i x_N)]\,\mathrm{d}x_i/\mathrm{d}T$.[27,30,46] We can relate the rigorous expression from eq 3 to the expression in the literature by

$$\alpha_{T,i} = \sum_{j=1}^{N-1}\frac{x_j}{x_i}\frac{D_{ij}^{\mathrm{M}}}{D_{ii}^{\mathrm{M}}}\alpha'_{T,i} \quad (i = 1, 2 \ldots N-1) \tag{4}$$

For a binary mixture, $\alpha_{T,i} = \alpha'_{T,i}$. Note that according to the definition of eq 3, the thermodynamic factor does not appear in the expression

https://doi.org/10.1021/acssuschemeng.3c05269
ACS Sustainable Chem. Eng. 2023, 11, 17086−17097

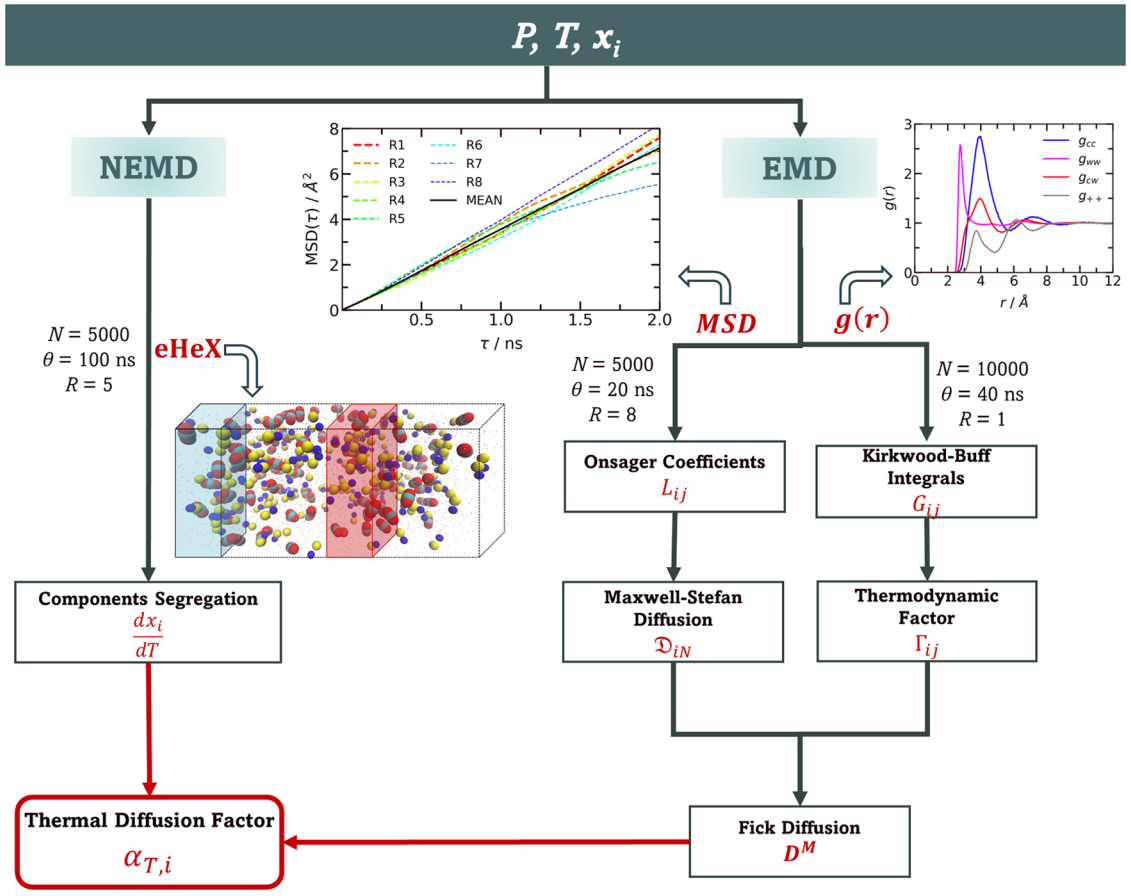

Figure 1. Framework to compute the thermodiffusion factor in multicomponent mixtures from molecular dynamics simulations. For each simulation, the number of molecules N, the total simulation time θ, and the number of independent simulations R are specified. Typical mean-squared displacement and radial distribution function plots and initial configurations for the eHeX method are shown.

for the thermal diffusion factor for binary mixtures. In multicomponent mixtures, $\alpha_{T,i}$ depends on Fickian diffusion coefficients to account for the cross diffusion. For a ternary mixture containing CO_2, NaCl, and H_2O, the thermal diffusion factors of CO_2 (α_{T,CO_2}) and NaCl ($\alpha_{T,NaCl}$) are expressed as

$$\alpha_{T,\mathrm{CO_2}} = -\frac{T}{x_c x_w}\left(\frac{\mathrm{d}x_c}{\mathrm{d}T} + \frac{D_{cs}^{M}}{D_{cc}^{M}}\frac{\mathrm{d}x_s}{\mathrm{d}T}\right) \tag{5}$$

$$\alpha_{T,\mathrm{NaCl}} = -\frac{T}{x_s x_w}\left(\frac{D_{sc}^{M}}{D_{ss}^{M}}\frac{\mathrm{d}x_c}{\mathrm{d}T} + \frac{\mathrm{d}x_s}{\mathrm{d}T}\right) \tag{6}$$

in which water is the reference component and subscripts c, s, and w stand for CO_2, salt, and water, respectively.

Alternatively, thermodiffusion may also be quantified by the Soret coefficient S_T, which relates to the thermodiffusion factor by $S_{T,i} = \alpha_{T,i}/T$. In our work, to compute both the Soret coefficient and thermal diffusion factor, we use prefactors in molar basis fixing the Nth component as reference ($x_i x_N$). Following our approach, the thermodiffusion coefficients are dependent on the choice of the concentration basis and the reference selected for ternary and higher multicomponent mixtures. A frame invariant prefactor definition could also be applied to remove this dependency;[51,52] however, the physical meaning of the thermal diffusion factor from eq 3 would be affected.

We simulated the thermodiffusion and compute the diffusion coefficients to evaluate the thermal diffusion factors under various conditions. Figure 1 presents a scheme of the framework proposed to determine $\alpha_{T,i}$ from the MD simulations.

NEMD Simulations. Thermodiffusion is simulated with non-equilibrium molecular dynamics through boundary-driven methods to estimate the segregation of each component with a temperature gradient. A thermostat can be used to represent thermodiffusion in NEMD simulations. To minimize the disturbance that the Langevin thermostat causes in the mixture dynamics, a larger damp factor may be required, which slows down the method convergence.[25] Therefore, we select the eHeX method,[53] an enhanced version of the HeX method,[23] to represent the Soret effect.

Two regions within the simulation box are selected to represent the hot and cold domains. In the eHeX method, kinetic energy is removed and added to the cold and hot regions, respectively, by rescaling and shifting the velocity of the particles at each time step, generating a constant heat flux. The simulation box is subdivided into 128 bins in the z direction (the same as the heat flux). The hot and cold regions are represented by 16 bins each. A large temperature gradient is required to magnify the Soret effect signal; as long as a linear profile of temperature is established in the steady-state regime, the local equilibrium assumption is met. The temperature difference between the hot and cold regions is set to approximately 50 K. After some simulation time, temperature and concentration gradients are established, and derivatives $\mathrm{d}x_i/\mathrm{d}T$ may be computed, excluding the thermal slabs and half of their sizes adjacent to them.

EMD Simulations. The direct estimation of Fickian diffusion coefficients from NEMD simulations requires pronounced concentration gradients, making the approach impractical.[54] In our work, we compute the Fickian diffusion coefficients from equilibrium molecular dynamics simulations indirectly by the Onsager coefficients L_{ij} and thermodynamic factors Γ_{ij}

$$[\boldsymbol{D}^{M}] = [\boldsymbol{\Delta}][\boldsymbol{\Gamma}] \tag{7}$$

where matrix $[\boldsymbol{\Delta}]$ represents a combination of the Onsager coefficients derived from the Maxwell–Stefan approach[55]

https://doi.org/10.1021/acssuschemeng.3c05269
ACS Sustainable Chem. Eng. 2023, 11, 17086−17097

$$\Delta_{ij} = (1 - x_i)\left(\frac{L_{ij}}{x_j} - \frac{L_{iN}}{x_N}\right) - x_i \sum_{k=1,k\neq i}^{N}\left(\frac{L_{kj}}{x_j} - \frac{L_{kN}}{x_N}\right) \quad (8)$$

Via MD, the Onsager coefficient L_{ij} is obtained from the mean-squared displacement MSD_{ij} of component i from component j

$$L_{ij} = \lim_{\tau\to\infty}\frac{1}{6N\tau}\left\langle\left[\sum_{l=1}^{N_i}(\mathbf{r}_{l,i}(t+\tau) - \mathbf{r}_{l,i}(t))\right]\cdot \left[\sum_{k=1}^{N_j}(\mathbf{r}_{k,j}(t+\tau) - \mathbf{r}_{k,j}(t))\right]\right\rangle = \lim_{\tau\to\infty}\frac{MSD_{ij}}{\tau} \quad (9)$$

where N, N_i, and N_j are the total number of components, the number of components i and j, respectively, and r_i is the position vector of component i. The Onsager coefficient is the slope of MSD_{ij} vs τ. The regression region must be linear, and τ should be large enough to guarantee that the molecules are in the diffuse regime.[56] The Maxwell−Stefan diffusion coefficients, which consider the chemical potential gradient as the diffusion driven force, can be estimated directly from the Onsager coefficients[57] (more details are in the Supporting Information).

Fickian diffusion may be affected by the finite-size simulation box.[58] Omrani et al.[59] have shown that the finite-size correction for CO_2 diffusivity into brine is two orders of magnitude lower than the diffusivity itself, probably due to the relatively higher viscosity of the mixture compared to gases, for instance. Because our system size is similar to theirs, we do not account for finite-size effects.

The thermodynamic factor is estimated from MD simulations through the Kirkwood−Buff integral (KBI) G_{ij}, which represents the depletion or excess of molecules i around molecule j.[60−62] The equations that express the thermodynamic factors from KBIs for a ternary mixture[54,63] are described in the Supporting Information. In the canonical ensemble, KBIs are determined by integrating the radial distribution functions $g_{ij}(r)$. The simple truncation in the integral leads to large deviations because KBIs are derived for infinite systems.[61] The thermodynamic limit of KBI may be obtained by computing G_{ij}^V for various open and finite subvolumes embedded in the closed simulation box and then extrapolating to infinite volume[64]

$$G_{ij}^V(L) = \int_0^L [g_{ij}(r) - 1]w(x)4\pi r^2 dr \quad (10)$$

$$G_{ij}^V(L) = G_{ij} + \frac{F_{ij}^{\infty}}{L} \quad (11)$$

in which $w(x) = 1 - 1.5x^2 + 0.5x^3$ for three-dimensional (3D) spherical subvolumes, where $x = r/L$, and L represents the subvolume diameters. The Kirkwood−Buff integral is obtained by the intercept of the linear region of the G_{ij}^V vs $1/L$ plot or, alternatively, the slope of the $G_{ij}^V L$ vs L plot, which usually gives a more clear linear region.[64] The $g_{ij}(r)$ for each subvolume is corrected to achieve convergence.[65]

Strong salts, such as NaCl, dissociate into electrolytes in an aqueous solution. The convenient way to report properties when there is only one salt in solution is on a salt basis. From MD simulations, the trajectory of single ions is available and can be manipulated to represent the salt property. The transformation of radial distribution functions and Onsager coefficients from ionic to salt basis is described in the Supporting Information.

Simulation Details. In our simulations, the nonbonded interactions between particles accounted for the van der Waals and electrostatics interactions, which are represented by the Lennard−Jones (LJ) and Coulombic potential, respectively. For the Soret effect in the CO_2−H_2O mixture, a set of force field combinations gave similar results.[25] In our work, the force fields for CO_2 and H_2O molecules were EPM2[66] and SPCE,[67] both semiflexible (fixed bond length but a harmonic potential for the angles). For the ions (Li^+, Na^+, K^+, Cl^-), classical integer-charge force fields was chosen.[68−70] Lorentz−Berthelot combining rules were applied to all LJ cross interactions. For verification, we computed CO_2 Fickian diffusion in water and compared with experimental data. To verify the force field for salts, NEMD simulations of the thermodiffusion of the salt−water mixture were performed, and the thermal diffusion factor was computed and compared with experimental data and MD results at the same conditions.[40,71]

The reference condition was chosen to be at 350 K, 400 bar, and CO_2 and NaCl concentrations (m_s) of 0.02 in mole fraction and 2 mol·kg^{-1}, respectively. To evaluate the effect of temperature, brine concentration, and composition, the mixture was also evaluated at different temperatures and salinities and with KCl and LiCl instead of NaCl. The molecules were placed randomly in the simulation box with an initial density of 1100 kg·m^{-3} for all simulations.

All simulations were performed in LAMMPS.[72] First, an equilibration was performed in the NPT ensemble for 1 ns to let the mixture be close to the desired pressure and temperature. A Nosé−Hoover thermostat and barostat were applied with time constants of 0.1 and 1 ps, respectively. Periodic boundary conditions were applied in all directions; the time step for the integration of Newton's equation was set to 2 fs. The constraint in bond length was implemented with the Rattle algorithm.[73] The LJ interaction cutoff was set at 1.2 nm. The long-range electrostatic interactions were computed using the particle−particle/particle-mesh (PPPM) algorithm[74] beyond 1.2 nm.

In the NEMD simulations, 5000 molecules were placed in an orthorhombic box, which has a length in the z direction twice longer than the other two directions ($L_z/L_y/L_x$ = 2:1:1). The cold and hot slab locations were chosen to avoid contact between them in the periodic images. The eHeX method was performed for 100 ns, from which the first 5 ns was for the equilibration. The sampling and the error were determined based on five independent simulations with different initial configurations. The pressure was not controlled during the NEMD simulations (fixed volume) and fluctuated around the target value. We considered the mean pressure as the one equilibrated in the initial NPT ensemble.

For the computation of KBIs, larger systems are required to guarantee convergence in the thermodynamic limit.[54] For the estimation of the Onsager coefficients, the number of uncorrelated positions is essential to use multiple time origins, which can be done in a long single simulation or in shorter sets of simulations.[56] Therefore, we calculated L_{ij} and G_{ij} values in different EMD simulations. To compute the Kirkwood−Buff integrals, we performed a single simulation with 10,000 molecules in a cubic box for 40 ns. The determination of Onsager coefficients was made based on eight independent 20 ns long simulations with 5000 molecules each. All EMD simulations were performed in the NVT ensemble after equilibration. The resulting thermodynamic factors were compared with the thermodynamic factor from the e-CPA equation of state.[75] Beyond the physical interaction, the e-CPA accounts for the association between water molecules, the Debye−Hückel interaction due to the long-range electrostatic interactions, and the Born interaction due to the solvation effect.[75−77]

RESULTS AND DISCUSSION

Force Field Validation. The EPM2 CO_2 and SPCE water force fields were validated by computing the Fickian diffusion coefficients in a wide range of temperatures. Our results were compared with experimental data in the literature,[78,79] MD simulations,[59] and a regression model[79] (Figure 2A). The data were obtained at various pressures. Although CO_2 diffusion slightly enhances with pressure, the effect is rather small when compared with the temperature effect.[79] Our MD results captured the exponential dependency of the temperature on the diffusion coefficient and were in good agreement with the literature. The MD CO_2 diffusion coefficients from Omrani et al.[59] captured the trend with temperature, but even at a lower pressure (100 bar), it consistently overestimated the diffusivity.[59] Omrani et al.[59] assumed that the thermodynamic

https://doi.org/10.1021/acssuschemeng.3c05269
ACS Sustainable Chem. Eng. 2023, 11, 17086−17097

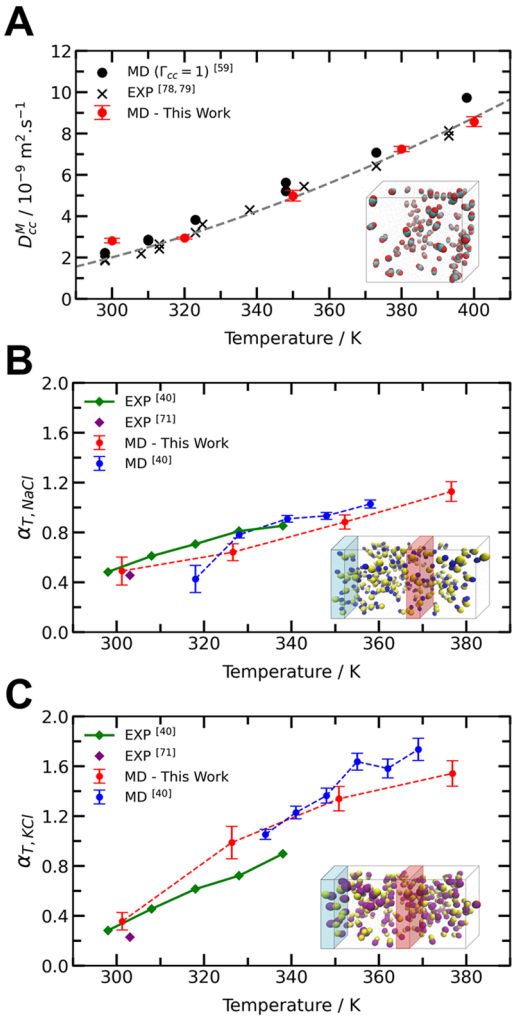

Figure 2. MD simulations to validate the selected force fields: (A) Fickian diffusion coefficient of CO_2 in water, at P = 400 bar, and x_{CO_2} = 0.02. Comparison with experimental data,[78,79] previous MD simulations,[59] and a regression model from an experimental data set[79] (dashed gray line). Thermal diffusion factor of (B) NaCl and (C) KCl in water, at P = 500 bar, and m_s = 2 mol·kg^{-1}. Comparison with previous MD simulations[40] and experimental data.[40,71] Typical MD initial configurations are shown for each property in the respective plot. The red, cyan, dark blue, and yellow spheres represent oxygen, carbon, sodium, and chloride atoms, respectively, and the gray dots represent water molecules.

factor is one, not accounting for nonideality. From MD simulations and the CPA EoS, however, we showed that the thermodynamic factor is lower than 1.[25] Therefore, improved predictions on the CO_2 diffusivity were obtained by accounting for the mixture nonideality.

To validate the force field choice for the electrolytes, we evaluated the thermodiffusion for the salt-H_2O mixtures. The thermal diffusion factor of NaCl and KCl from our simulations were compared with the MD simulations from Römer et al.[40] and experimental data[40,71] at similar conditions (Figure 2B,C, respectively). Our MD simulations were in good agreement both in value and trend with the previous work. The uncertainty in our MD simulations could be decreased by sampling more independent simulations or increasing the thermal gradient.

In the temperature range from our investigation, the salt thermal diffusion factor is positive, and the ions accumulate on the cold side. Salts become more thermophobic by increasing the temperature, and one expects a sign inversion in the Soret coefficient at temperatures lower than 300 K.[42] Römer et al.[40] argued that the Soret coefficient sign inversion is related to the water hydrogen bond network. At lower temperatures, the mixture free energy is minimized, with H_2O molecules accumulating in the cold region where the hydrogen bonds are more organized. By increasing temperature, the hydrogen bond network is disturbed; at this condition, the accumulation of water on the hot side increases the entropy, which leads to a lower mixture free energy.[40] Römer et al.[40] did not correlate the thermal diffusion factor sign inversion with the water−ion solvation and hydrogen bond structures from the MD radial distribution functions.[40]

We also computed the thermal diffusion factor for LiCl in water. To the best of our knowledge, the reported experimental data covered only temperatures lower than 300 K.[80,81] At T = 270 K, P = 1 bar, and m_s = 1.85 mol·kg^{-1}, from MD simulations, $\alpha_{T,LiCl} = -0.62 \pm 0.07$, and the electrolyte concentrated in the hot region. From experiments, $\alpha_{T,LiCl} = -0.98$,[81] and the same trend with temperature as the other alkali halide salts was observed. Our MD simulations captured the thermophilic nature of LiCl but underestimated the magnitude of the LiCl thermal diffusion factor by 37% at low temperatures. The same underestimation was reported by Di Lecce and Bresme.[42] Because our simulations of brine with CO_2 were performed at higher temperatures, we kept the same force field for Li^+ in the simulations.

Thermal Diffusion Factor of CO_2 in NaCl Brine. The application of the method proposed in Figure 1 is shown in Figure 3 for the CO_2−NaCl-H_2O mixture. From the NEMD simulations, we obtained the temperature profile and the segregation of CO_2 and NaCl in the simulation box (Figure 3A). In the simulations, we applied a thermal gradient at mean temperatures of 300, 350, and 400 K. The same plots at mean temperatures of 320 and 380 K are shown in Figure S2 in the Supporting Information. Although a pronounced temperature gradient was applied, the temperature profile was linear between the thermal regions and the local equilibrium was met.

At 300 K, CO_2 accumulates in the cold region, whereas at 400 K, it accumulates in the hot side, indicating an inversion in the Soret effect with temperature. The temperature of inversion is around 350 K since there is almost no detectable CO_2 segregation under this condition. The CO_2 migration trend from thermophobic to thermophilic is also observed by increasing temperature in the binary CO_2−H_2O mixture.[25] Without salt in the mixture, inversion occurs at a higher temperature (around 400 K).

As in the binary NaCl−H_2O (Figure 2B), electrolytes accumulate in the cold region in the CO_2−NaCl−H_2O mixture. The higher the temperature, the more pronounced the salt segregation. Therefore, while CO_2 becomes more thermophilic, NaCl becomes more thermophobic by increasing the temperature.

To compute the thermal diffusion factors, we computed the structural and dynamic properties. Figure 3B shows the thermodynamic factor matrix elements for various temperatures. The continuous lines represent the thermodynamic factors from e-CPA.[75] Overall, we found good agreement between MD and e-CPA results: $\Gamma_{ss} > \Gamma_{cc} > \Gamma_{sc} > \Gamma_{cs}$, and the thermodynamic factors were nearly temperature-independent. The further the Γ_{ij} from the unity value, the more nonideal the mixture between species.[61] Salt−water interactions are stronger

https://doi.org/10.1021/acssuschemeng.3c05269
ACS Sustainable Chem. Eng. 2023, 11, 17086−17097

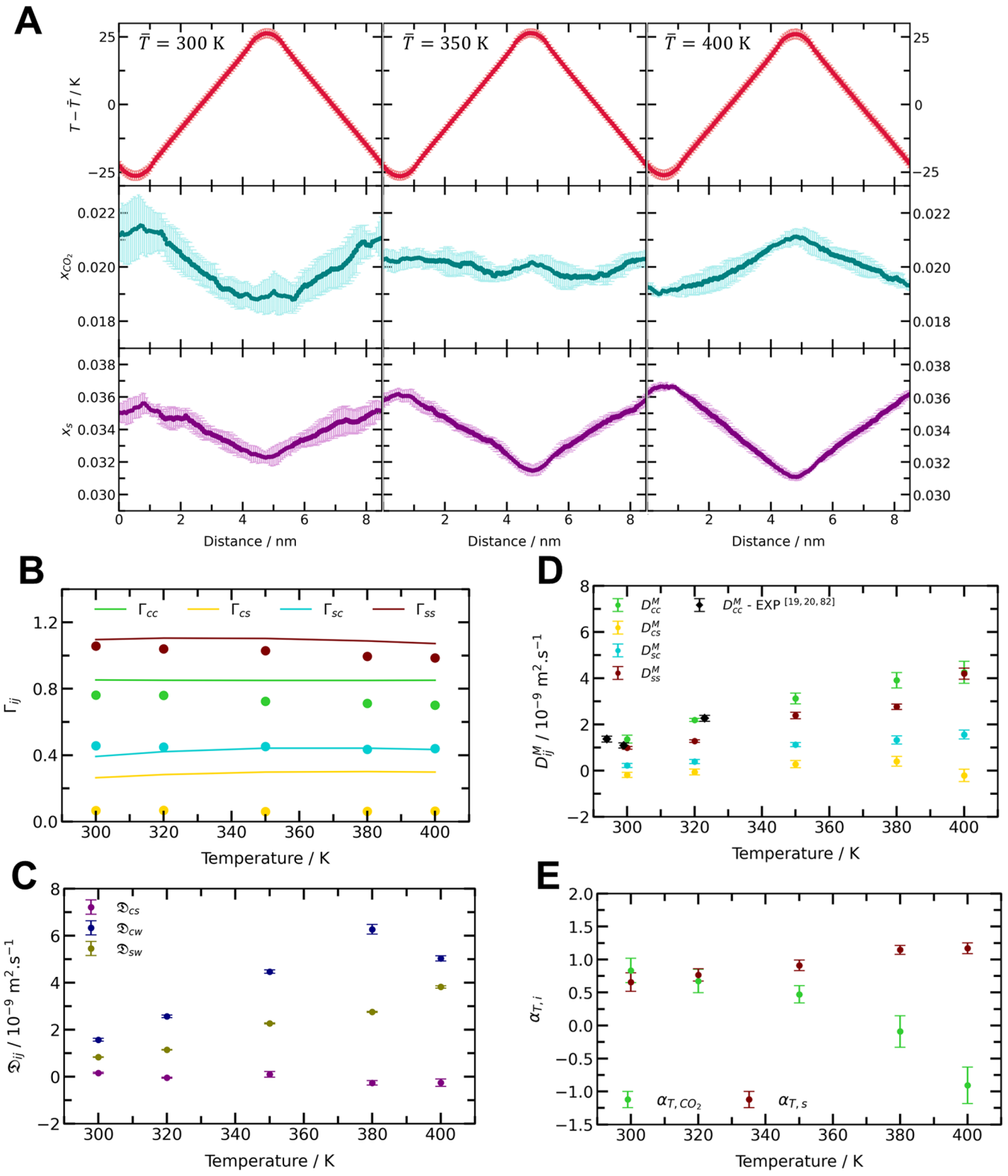

Figure 3. MD simulation outcomes based on our proposed framework to compute the thermal diffusion factor of the CO_2−NaCl−H_2O mixture at P = 400 bar, x_{CO_2} = 0.02, and m_s = 2 mol·kg^{-1}.(A) Temperature gradient and CO_2 and NaCl segregation in the simulation box at three mean temperatures ($\bar{T}$). (B) Thermodynamic factors; the continuous line and the dots represent the thermodynamic factor from the e-CPA EoS and MD simulations, respectively. (C) Maxwell−Stefan diffusion coefficients. (D) Fickian diffusion coefficients; the black dots represent experimental data from the CO_2 diffusion in brine at similar conditions.[19,20,82] (E) Thermal diffusion factors of CO_2 and NaCl.

than salt−salt interactions ($\Gamma_{ss} > 1$), whereas the interaction between CO_2 and water is weaker than CO_2−CO_2 interactions ($\Gamma_{cc} < 1$).[62] The lower thermodynamic factor between the salt and CO_2 indicates repulsion interactions between these two species. The lower affinity of CO_2 toward brine reduces its solubility, for instance.[12]

https://doi.org/10.1021/acssuschemeng.3c05269
ACS Sustainable Chem. Eng. 2023, 11, 17086−17097

From the Onsager coefficients based on the mean-squared displacement, we computed the Maxwell–Stefan diffusion coefficients $\mathcal{D}_{ij}$ (Figure 3C). The mobility of species increases with temperature, and as a consequence, the diffusivities of CO_2 and NaCl in water increase. On the other hand, the Maxwell–Stefan diffusion coefficient between CO_2 and NaCl fluctuates around zero; the chemical potential gradient from one does not induce a pronounced mass flux from the other. A negative $\mathcal{D}_{cs}$ neither represents a physical inconsistency nor violates irreversible thermodynamics theory and is in fact common for electrolytes containing mixtures.[83]

From the thermodynamic factors and Onsager coefficients, we determined the Fickian diffusion coefficients (Figure 3D). The main diffusivity of CO_2 and NaCl increases with increasing temperature. For validation, we compared the CO_2 diffusion with experimental data at similar conditions.[19,20,82] A good agreement was found between the experiments and MD simulations. Some elements of the Fickian diffusion matrix are negative, which means cross diffusion of one component may be induced in the direction where the other component concentration is higher, representing the nonideality of the mixture; because the matrix determinant is always positive, this does not represent an inconsistency.[26] The cross-diffusion coefficients are smaller than the main-diffusion coefficients, but they are not negligible, especially the induced salt diffusion by the CO_2 concentration (D_{sc}^{M}). Therefore, the coupled mass flux should be accounted for in the thermal diffusion computation.

We determined the thermal diffusion of CO_2 and NaCl in the mixture (Figure 3E) using eqs 5 and 6, respectively, by combining the concentration segregation with temperature from Figure 3A and the diffusivities from Figure 3D. At 300 K, CO_2 and NaCl have a similar magnitude of thermodiffusion. By increasing the temperature, the CO_2 thermal diffusion factor decreases, whereas $\alpha_{T,NaCl}$ increases. The temperature dependency is stronger in the CO_2 Soret effect, and α_{T,CO_2} changes sign between 350 and 380 K. The trend for CO_2–NaCl–H_2O is the same as observed by Artola and Rousseau[45] for an ideal ternary mixture: the heavier (NaCl) and the lighter (H_2O) components enrich the cold and hot regions, respectively, whereas the intermediate (CO_2) component segregation changes depending on the conditions.

Figure S3 and Table S1 of the Supporting Information show the comparison between thermal diffusion factors with and without cross-diffusion effects. The trends presented by both approaches are similar; however, there are some deviations when the segregation (dx_i/dT) of the other component is pronounced. For instance, we showed the thermal diffusion factors at an even higher temperature (500 K), where $\alpha_{T,CO_2} = 1.79 \pm 0.35$ and $\alpha'_{T,CO_2} = -2.65 \pm 0.11$, which represents a deviation of 48%. The magnitude of the thermal diffusion factor accounting for the cross-diffusion effect is lower than $\alpha'_{T,i}$ because CO_2 and NaCl concentrate in different regions (opposite dx_i/dT) at higher temperatures. We expected an even more pronounced deviation at higher temperatures for superhot geothermal formations.

Salt Concentration Effect. To evaluate the effect of brine concentration on CO_2 thermodiffusion, we applied the framework from Figure 1 with m_s = 0, 1, and 2 mol·kg^{-1}. The temperature and concentration profiles at this condition are shown in Figure S4 of the Supporting Information. We compared the CO_2 segregation due to the thermal gradient at mean temperatures of 300, 350, and 400 K, at two salinities, and without electrolytes in the mixture (Figure 4A). In all cases, the CO_2 concentration on the cold side decreases by increasing the mean temperature. CO_2 becomes more thermophilic in the presence of electrolytes; the more concentrated the brine, the less thermophobic the CO_2 in the mixture.

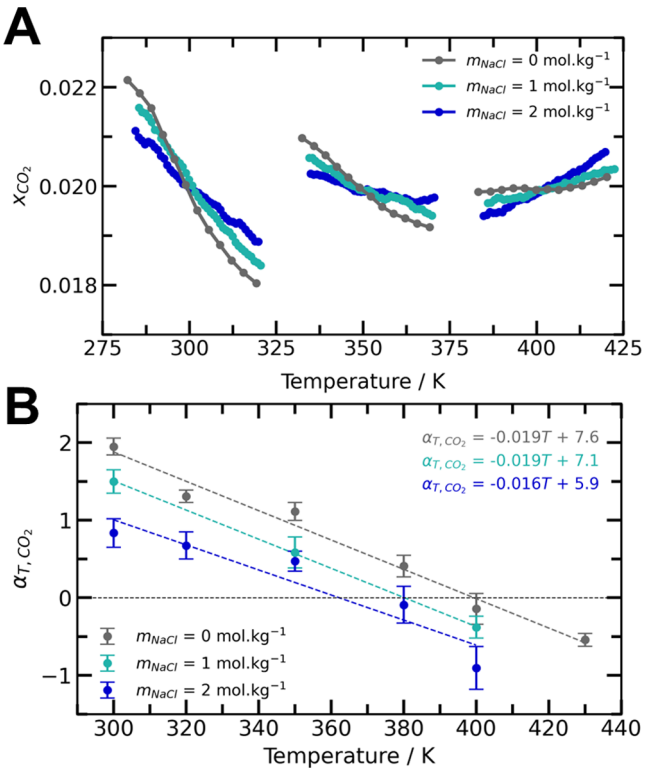

Figure 4. (A) CO_2 segregation in brine vs temperature at $\bar{T}$ = 300, 350, and 400 K; P = 400 bar; x_{CO_2} = 0.02; and m_s = 0, 1, 2 mol·kg^{-1}. (B) CO_2 thermal diffusion factor in brine vs mean temperature at the same conditions as in (A); the dashed line represents a linear interpolation, as shown in the legend.

From the thermodynamic factors and diffusion coefficients (Figure S5 of the Supporting Information), we computed the CO_2 thermal diffusion factor at different temperatures and salinities (Figure 4B). We also computed the α_{T,CO_2} at a higher temperature (430 K) in the CO_2–H_2O mixture to demonstrate that there is an inversion in the Soret effect without brine. The electrolytes decrease the temperature of inversion, where CO_2 becomes thermophilic. By linear interpolation, the rate of decrease of α_{T,CO_2} is almost independent of brine salinity; the inversion temperature is approximately 400, 380, and 358 K at m_s = 0, 1, and 2 mol·kg^{-1}, respectively.

To better understand the role of electrolytes in CO_2 dynamics, we computed radial distribution functions between the components of the mixture at various temperatures and brine concentrations (Figures S6 and S7, respectively, of the Supporting Information). The H_2O–H_2O interactions were affected by both the temperature and electrolytes, whereas the CO_2–CO_2 interactions were enhanced. Part of the water molecules were found within the hydration shells shielding the ions, which disturb locally the hydrogen bond tetrahedral structures (Figure 5B) and decrease the medium permittivity—dielectric saturation.[84,85] There are repulsion interactions between CO_2 and the electrolytes, and by increasing the

https://doi.org/10.1021/acssuschemeng.3c05269
ACS Sustainable Chem. Eng. 2023, 11, 17086–17097

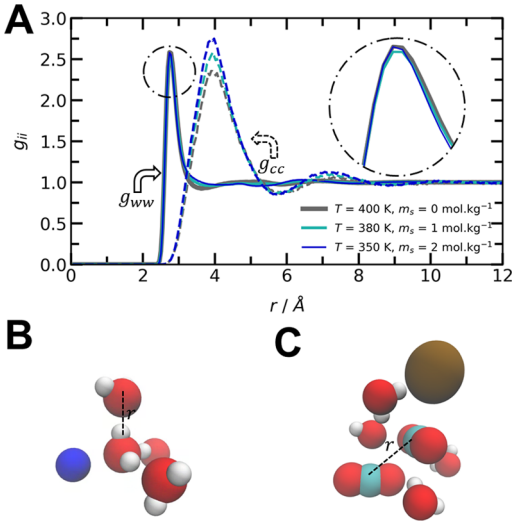

Figure 5. (A) Radial distribution function between CO_2 molecules (dashed lines) and H_2O molecules (solid lines) close to the α_{T,CO_2} inversion temperature P = 400 bar, x_{CO_2} = 0.02, and m_s = 0, 1, 2 mol·kg^{-1}. The g_{ww} first peak is highlighted by the dotted solid circle for better visualization. Representation of the self-interaction between (B) water and (C) CO_2 molecules in the presence of electrolytes. The red, white, cyan, dark blue, and yellow spheres represent oxygen, hydrogen, carbon, sodium, and chloride atoms, respectively.

salinity, CO_2 molecules tend to interact stronger with other CO_2 molecules (Figure 5C)—salt-out effect.[12] The cation hydration and CO_2−H_2O tetrel bond interactions decrease with temperature and are almost salinity-independent. With ions less solvated by water at higher temperatures, the ionic association and the repulsion between CO_2 and the cation increase. CO_2 interactions with other CO_2 molecules are stronger than those with H_2O molecules ($\Gamma_{cc} < 1$).

Because both CO_2−CO_2 and H_2O−H_2O interactions exhibit the same behavior with temperature and salinity, we investigated these interactions at m_s = 0, 1, and 2 mol·kg^{-1} close to the respective temperature of inversion (Figure 5A). The effect of salinity on the CO_2−CO_2 interactions is stronger than the effect of temperature. Nevertheless, at the inversion temperature from the three salinity conditions, the structures of water molecules (H_2O−H_2O interactions) are almost identical. Therefore, the hydrogen bond network controls the Soret effect of CO_2 in an aqueous mixture. The more organized the water structures, the more thermophobic the CO_2, and by disturbing these structures, either by increasing temperature or salinity, CO_2 becomes more thermophilic.

Effect of Type of Salt. The effect of type of salt was evaluated by computing the thermodiffusion for different cations. Besides Na^+, we focused on the alkali halide salts composed of K^+ and Li^+. CO_2 segregation by thermal gradient in the KCl and LiCl brine (Figures S8 and S9, respectively, of the Supporting Information) follows the same trend as in the NaCl brine. CO_2 is thermophobic at 300 K but thermophilic at higher temperatures.

The structural and dynamic properties were computed for each brine composition (Figures S10 of the Supporting Information). Overall, alkali metal brine increases the nonideal behavior of CO_2 in the mixture and decreases the CO_2 diffusivity; Na^+ brine has the most pronounced effect on CO_2 thermodynamic factor and Fickian diffusion coefficient. LiCl is the least thermophobic salt, and an inversion in the Soret effect is expected close to 300 K. As in the brine mixture without CO_2,[40−42] the temperature increases the salt thermophopicity; KCl brine has the most pronounced dependency on temperature.

From component segregation and Fickian diffusivity, we computed the CO_2 thermal diffusion factor from each type of salt (Figure 6A). All brine compositions reduced the CO_2 thermal diffusion factor compared with the condition without salt. As in the structural and dynamic properties, the effect of Na^+ was the most pronounced. An inversion in the Soret effect was also expected for KCl and LiCl close to 380 and 390 K, respectively.

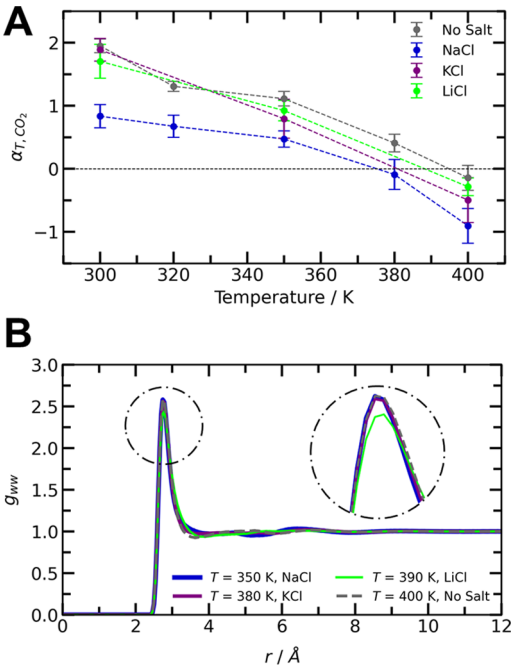

Figure 6. CO_2 Soret effect for different brines (NaCl, KCl, LiCl) and water (no salt) at P = 400 bar, x_{CO_2} = 0.02, and m_s = 2 mol·kg^{-1}. (A) CO_2 thermal diffusion factor vs temperature. (B) Radial distribution function between H_2O molecules close to the α_{T,CO_2} inversion temperature of each brine type. The g_{ww} first peak is highlighted by the dotted solid circle for better visualization.

We investigated how the brine cation affects the molecular structure in the mixture (Figure S11 of the Supporting Information). The smallest cation (Li^+) has the strongest hydration, whereas the largest (K^+) has the weakest; the smaller the ion, the stronger the electrostatic potential on its surface. The coordination numbers of water molecules surrounding Li^+, Na^+, and K^+ in the first solvation shell are 4.0, 5.4, and 6.4, respectively, which are in good agreement with the MD results at similar conditions from Di Lecce and Bresme.[42] One could expect more water hydrogen bond network disturbance for cations with a more pronounced hydration energy. Nevertheless, smaller cations such as Li^+ have fewer water molecules surrounding them, which limits the effect on water self-association. Therefore, Na^+, the cation with intermediate size and hydration energy, has the largest impact on the water hydrogen bond network structure. The ionic association and clusterization are stronger in the KCl brine because the weaker cation solvation increases the ion−ion interaction, as can be

https://doi.org/10.1021/acssuschemeng.3c05269
ACS Sustainable Chem. Eng. 2023, 11, 17086−17097

seen in the first well-defined peak of the K^+-K^+ and K^+-Cl^- radial distribution functions. The repulsion between CO_2 and the cation is stronger with NaCl; therefore, the CO_2-CO_2 interactions are enhanced in brine with Na^+.

We computed the radial distribution functions of water molecules at the same salinity (2 mol·kg^{-1}) for different brines and with no salt at the respective temperature of inversion (Figure 6B). The water molecules in the mixtures with NaCl, KCl, and no salt present similar self-association structures at the temperature of inversion, as expected by our initial hypothesis. However, the LiCl brine presents a higher degree of disturbance in the hydrogen bond network at the temperature of inversion. As seen from Figure 6A, the order of CO_2 thermal diffusion between Li^+ and K^+ changes with increasing temperature. The anomalous behavior in the LiCl brine may be related to the stronger hydration energy of Li^+. The Li^+ force field may be also not a good representation for the cation; because no experimental data is available at higher temperatures, we have not validated the $LiCl-H_2O$ Soret effect as we have done for NaCl and KCl. The hydrogen bond network structure may be insufficient to describe the CO_2 Soret effect when using different brines. Salt specificity may affect the mixture in a complex way; by changing the salt type, it also changes, for instance, the ionic association, hydration, and clusterization.

CONCLUSIONS

We evaluated the effect of salinity on CO_2 thermodiffusion in brine. The main findings of our work are summarized as follows

1. A methodology is introduced to compute the thermal diffusion factor in multicomponent mixtures using molecular dynamics simulations. In mixtures with more than two components, cross diffusion may be significant. Consequently, the thermal diffusion factor may depend on diffusion coefficients. The extension of the cross-diffusion effect on thermodiffusion depends on the mixture conditions. From nonequilibrium molecular dynamics simulations, one computes the derivatives of concentration with temperature for each component; from equilibrium molecular dynamics, Fickian diffusivities are computed.
2. CO_2 is thermophobic at lower temperatures and may become thermophilic by increasing temperature. The same trend is observed with and without salts. Salts may decrease the Soret inversion temperature.
3. The water self-association structures affect the region where CO_2 accumulates. Stronger hydrogen bond networks lead to a more thermophobic CO_2. Increasing the salt concentration disturbs the hydrogen bonds and CO_2 becomes more thermophilic.
4. Different alkali metal cations have different effects on the CO_2 thermodiffusion. Brines containing either K^+ or Na^+ cations have the same water structure at their respective temperatures of inversion; however, the same may not apply to the brine with Li^+. The hydrogen bond disturbance hypothesis may not describe the salt specificity effect on the CO_2 thermal diffusion factor, especially for cations with pronounced hydration energy. In future work, a better understanding of the role of different cations in the Soret effect may be pursued.

Our work sets the stage for more rigorous modeling of species distribution in subsurface formations. By investigating the diffusion and thermodiffusion of CO_2 in the brine, we expand the knowledge of CO_2 distribution in deep saline aquifers and geothermal formations.

Temperature may have a substantial effect on the level of CO_2 segregation. In some geothermal formations, the temperature can be very high, and the CO_2-H_2O mixture could be in the supercritical condition. In future work, we plan to use the theoretical framework presented in this work to investigate the distribution of CO_2 in aqueous mixtures under supercritical conditions by thermodiffusion and gravity segregation.

ASSOCIATED CONTENT

Supporting Information

The Supporting Information is available free of charge at https://pubs.acs.org/doi/10.1021/acssuschemeng.3c05269.

Methodology to compute the thermodynamic factor from the Kirkwood−Buff integral for a ternary mixture; methodology to transform MD ionic properties into salt basis; temperature and component segregation profiles at different temperatures, salt concentrations, and brine compositions; thermodynamic factor, diffusivity, and salt thermal diffusion factor for different salt concentrations and brine compositions; and effect on temperature, salinity, and brine composition on molecules' radial distribution functions (ZIP)

AUTHOR INFORMATION

Corresponding Author

Abbas Firoozabadi − *Department of Chemical and Biomolecular Enginering, Rice University, Houston, Texas 77005, United States;* orcid.org/0000-0001-6102-9534; Email: af@rerinst.org

Authors

Felipe Mourao Coelho − *School of Chemical Engineering, University of Campinas, Campinas, SP 13083-852, Brazil;* orcid.org/0000-0002-7572-1991

Luis Fernando Mercier Franco − *School of Chemical Engineering, University of Campinas, Campinas, SP 13083-852, Brazil*

Complete contact information is available at: https://pubs.acs.org/10.1021/acssuschemeng.3c05269

Notes

The authors declare no competing financial interest.

ACKNOWLEDGMENTS

The author thanks São Paulo Research Foundation (FAPESP) for the project funding (grant #2018/02713-8, #2020/13300-6, and #2021/13068-9) and the "Centro Nacional de Processamento de Alto Desempenho em São Paulo" (CENAPAD-SP) and the John David Rogers Computing Center (CCJDR) at the Institute of Physics "Gleb Wataghin" of the University of Campinas for providing computational resources.

REFERENCES

(1) Benson, S. M.; Surles, T. Carbon Dioxide Capture and Storage: An Overview With Emphasis on Capture and Storage in Deep Geological Formations. *Proc. IEEE* **2006**, *94*, 1795−1805.

(2) Bachu, S. CO_2storage in geological media: Role, means, status and barriers to deployment. *Prog. Energy Combust.* **2008**, *34*, 254−273.

(3) Boot-Handford, M. E.; Abanades, J. C.; Anthony, E. J.; Blunt, M. J.; Brandani, S.; Mac Dowell, N.; Fernández, J. R.; Ferrari, M.-C.;

Gross, R.; Hallett, J. P.; et al. Carbon capture and storage update. *Energy Environ. Sci.* **2014**, *7*, 130−189.
(4) Bachu, S.; Adams, J. Sequestration of CO_2 in geological media in response to climate change: capacity of deep saline aquifers to sequester CO_2 in solution. *Energy Convers. Manage.* **2003**, *44*, 3151−3175.
(5) Celia, M. A.; Bachu, S.; Nordbotten, J. M.; Bandilla, K. W. Status of CO_2 storage in deep saline aquifers with emphasis on modeling approaches and practical simulations. *Water Resour. Res.* **2015**, *51*, 6846−6892.
(6) Lelli, M.; Kretzschmar, T. G.; Cabassi, J.; Doveri, M.; Sanchez-Avila, J. I.; Gherardi, F.; Magro, G.; Norelli, F. Fluid geochemistry of the Los Humeros geothermal field (LHGF - Puebla, Mexico): New constraints for the conceptual model. *Geothermics* **2021**, *90*, No. 101983, DOI: 10.1016/j.geothermics.2020.101983.
(7) Ármannsson, H. Carbon Dioxide Emissions from Icelandic Geothermal Areas. *Procedia Earth Planet. Sci.* **2017**, *17*, 104−107.
(8) Randolph, J. B.; Saar, M. O. Coupling carbon dioxide sequestration with geothermal energy capture in naturally permeable, porous geologic formations: Implications for CO_2 sequestration. *Energy Proc.* **2011**, *4*, 2206−2213.
(9) Esteves, A. F.; Santos, F. M.; Pires, J. C. M. Carbon dioxide as geothermal working fluid: An overview. *Renewable Sustainable Energy Rev.* **2019**, *114*, 109331−109338, DOI: 10.1016/j.rser.2019.109331.
(10) Hu, J.; Duan, Z.; Zhu, C.; Chou, I.-M. PVTx properties of the CO_2-H_2O and CO_2-H_2O-NaCl systems below 647K: Assessment of experimental data and thermodynamic models. *Chem. Geo.* **2007**, *238*, 249−267.
(11) Trusler, J. M. Thermophysical Properties and Phase Behavior of Fluids for Application in Carbon Capture and Storage Processes. *Annu. Rev. Chem. Biomol.* **2017**, *8*, 381−402.
(12) Liu, Y.; Hou, M.; Yang, G.; Han, B. Solubility of CO_2 in aqueous solutions of NaCl, KCl, $CaCl_2$ and their mixed salts at different temperatures and pressures. *J. Supercrit. Fluids* **2011**, *56*, 125−129.
(13) Enick, R. M.; Klara, S. M. CO_2 Solubility in Water and Brine under Reservoir Conditions. *Chem. Eng. Commun.* **1990**, *90*, 23−33.
(14) Chalbaud, C.; Robin, M.; Lombard, J.-M.; Martin, F.; Egermann, P.; Bertin, H. Interfacial tension measurements and wettability evaluation for geological CO_2 storage. *Adv. Water Resour.* **2009**, *32*, 98−109.
(15) Aggelopoulos, C.; Robin, M.; Vizika, O. Interfacial tension between CO_2 and brine (NaCl+$CaCl_2$) at elevated pressures and temperatures: The additive effect of different salts. *Adv. Water Resour.* **2011**, *34*, 505−511.
(16) Mutailipu, M.; Liu, Y.; Jiang, L.; Zhang, Y. Measurement and estimation of CO2-brine interfacial tension and rock wettability under CO2 sub- and super-critical conditions. *J. Colloid Interface Sci.* **2019**, *534*, 605−617.
(17) Jiang, H.; Economou, I. G.; Panagiotopoulos, A. Z. Molecular Modeling of Thermodynamic and Transport Properties for CO2 and Aqueous Brines. *Acc. Chem. Res.* **2017**, *50*, 751−758.
(18) Cadogan, S. P.; Hallett, J. P.; Maitland, G. C.; Trusler, J. P. M. Diffusion Coefficients of Carbon Dioxide in Brines Measured Using 13C Pulsed-Field Gradient Nuclear Magnetic Resonance. *J. Chem. Eng. Data* **2015**, *60*, 181−184.
(19) Belgodere, C.; Dubessy, J.; Vautrin, D.; Caumon, M.-C.; Sterpenich, J.; Pironon, J.; Robert, P.; Randi, A.; Birat, J.-P. Experimental determination of CO_2 diffusion coefficient in aqueous solutions under pressure at room temperature via Raman spectroscopy: impact of salinity (NaCl). *J. Raman Spectrosc.* **2015**, *46*, 1025−1032.
(20) Perera, P. N.; Deng, H.; Schuck, P. J.; Gilbert, B. Diffusivity of Carbon Dioxide in Aqueous Solutions under Geologic Carbon Sequestration Conditions. *J. Phys. Chem. B* **2018**, *122*, 4566−4572.
(21) Köhler, W.; Morozov, K. I. The Soret effect in liquid mixtures - A review. *J. Non-Equilib. Thermodyn.* **2016**, *41*, 151−197, DOI: 10.1515/jnet-2016-0024.
(22) Hoang, H.; Galliero, G. Predicting thermodiffusion in simple binary fluid mixtures. *Eur. Phys. J. E* **2022**, *45*, No. 42, DOI: 10.1140/epje/s10189-022-00197-z.
(23) Hafskjold, B.; Ikeshoji, T.; Ratkje, S. K. On the molecular mechanism of thermal diffusion in liquids. *Mol. Phys.* **1993**, *80*, 1389−1412.
(24) Ghorayeb, K.; Firoozabadi, A.; Anraku, T. Interpretation of the Unusual Fluid Distribution in the Yufutsu Gas-Condensate Field. *SPE J.* **2003**, *8*, 114−123.
(25) Coelho, F. M.; Franco, L. F. M.; Firoozabadi, A. Thermodiffusion of CO_2 in Water by Nonequilibrium Molecular Dynamics Simulations. *J. Phys. Chem. B* **2023**, *127*, 2749−2760.
(26) Mutoru, J. M.; Firoozabadi, A. Form of multicomponent Fickian diffusion coefficients matrix. *J. Chem. Thermodyn.* **2011**, *43*, 1192−1203, DOI: 10.1016/j.jct.2011.03.003.
(27) Galliero, G.; Bataller, H.; Bazile, J. P.; et al. Thermodiffusion in multicomponent n-alkane mixtures. *NPJ Microgravity* **2017**, *3*, 20−27.
(28) Mialdun, A.; Bou-Ali, M.; Shevtsova, V. Soret vector for description of multicomponent mixtures. *Sci. Rep.* **2021**, *11*, No. 17735.
(29) Ryzhkov, I. I.; Shevtsova, V. M. On the Cross-diffusion and Soret Effect in Multicomponent Mixtures. *Microgravity Sci. Technol.* **2009**, *21*, 37−40.
(30) VanVaerenbergh, S.; Srinivasan, S.; Saghir, M. Z. Thermodiffusion in multicomponent hydrocarbon mixtures: Experimental investigations and computational analysis. *J. Chem. Phys.* **2009**, *131*, 114505−114508.
(31) Perronace, A.; Leppla, C.; Leroy, F.; Rousseau, B.; Wiegand, S. Soret and mass diffusion measurements and molecular dynamics simulations of n-pentane-n-decane mixtures. *J. Chem. Phys.* **2002**, *116*, 3718−3729.
(32) Perronace, A.; Ciccotti, G.; Leroy, F.; Fuchs, A. H.; Rousseau, B. Soret coefficient for liquid argon-krypton mixtures via equilibrium and nonequilibrium molecular dynamics: A comparison with experiments. *Phys. Rev. E* **2002**, *66*, 031201−031215.
(33) Rousseau, B.; Nieto-Draghi, C.; Avalos, J. B. The role of molecular interactions in the change of sign of the Soret coefficient. *Europhys. Lett.* **2004**, *67*, 976−982.
(34) Nieto-Draghi, C.; Ávalos, J. B.; Rousseau, B. Computing the Soret coefficient in aqueous mixtures using boundary driven nonequilibrium molecular dynamics. *J. Chem. Phys.* **2005**, *122*, 114503−114507.
(35) Galliero, G.; Volz, S. Thermodiffusion in model nanofluids by molecular dynamics simulations. *J. Chem. Phys.* **2008**, *128*, 064505−064508.
(36) Hannaoui, R.; Galliero, G.; Hoang, H.; Boned, C. Influence of confinement on thermodiffusion. *J. Chem. Phys.* **2013**, *139*, 114704−114707.
(37) Mozaffari, S. H.; Srinivasan, S.; Saghir, M. Z. Thermodiffusion in binary and ternary hydrocarbon mixtures studied using a modified heat exchange algorithm. *Therm. Sci. Eng. Prog.* **2017**, *4*, 168−174.
(38) Antoun, S.; Saghir, M. Z.; Srinivasan, S. An improved molecular dynamics algorithm to study thermodiffusion in binary hydrocarbon mixtures. *J. Chem. Phys.* **2018**, *148*, 104507−104511.
(39) Diaz-Marquez, A.; Stirnemann, G. In silico all-atom approach to thermodiffusion in dilute aqueous solutions. *J. Chem. Phys.* **2021**, *155*, 174503−174512.
(40) Römer, F.; Wang, Z.; Wiegand, S.; Bresme, F. Alkali halide solutions under thermal gradients: Soret coefficients and heat transfer mechanisms. *J. Phys. Chem. B* **2013**, *117*, 8209−8222.
(41) Di Lecce, S.; Albrechta, T.; Bresme, F. The role of ion-water interactions in determining the Soret coefficient of LiCl aqueous solutions. *Phys. Chem. Chem. Phys.* **2017**, *19*, 9575−9583.
(42) Di Lecce, S.; Bresme, F. Soret coefficients and thermal conductivities of alkali halide aqueous solutions via non-equilibrium molecular dynamics simulations. *Mol. Simul.* **2019**, *45*, 351−357.
(43) Rezende Franco, L.; Sehnem, A. L.; Neto, A. M. F.; Coutinho, K. Molecular dynamics approach to calculate the thermodiffusion (Soret

and Seebeck) coefficients of salts in aqueous solutions. *J. Chem. Theory Comput.* **2021**, *17*, 3539−3553, DOI: 10.1021/acs.jctc.1c00116.
(44) Hutchinson, A. J.; Torres, J. F.; Corry, B. Modeling thermodiffusion in aqueous sodium chloride solutionsWhich water model is best? *J. Chem. Phys.* **2022**, *156*, 164503−164512.
(45) Artola, P. A.; Rousseau, B. Isotopic Soret effect in ternary mixtures: Theoretical predictions and molecular simulations. *J. Chem. Phys.* **2015**, *143*, 174503−174509.
(46) Antoun, S.; Saghir, M. Z.; Srinivasan, S. Composition effect on thermophobicity of ternary mixtures: An enhanced molecular dynamics method. *J. Chem. Phys.* **2018**, *149*, No. 034502, DOI: 10.1063/1.5031004.
(47) Chen, X.; Liu, B.; Liang, R.; Xiao, S. Study of the pressure effect on the thermodiffusion behavior in multicomponent n-alkane mixtures by using non-equilibrium molecular dynamics. *Phys. Scr.* **2023**, *98*, 015411−015413.
(48) Hirschfelder, J.; Bird, R. B.; Curtiss, C. F. *Molecular Theory of Gases and Liquids*; Wiley: New York, 1954.
(49) De Groot, S.; Mazur, P. *Non-Equilibrium Thermodynamics*, 2nd ed.; Dover Publications: New York, 1984.
(50) Firoozabadi, A. *Thermodynamics and Applications in Hydrocarbon Energy Production*, 1st ed.; McGraw-Hill Education: New York, 2016.
(51) de Zárate, J. M. O. Definition of frame-invariant thermodiffusion and Soret coefficients for ternary mixtures. *Eur. Phys. J. E* **2019**, *42*, No. 43, DOI: 10.1140/epje/i2019-11803-2.
(52) de Zárate, J. M. O.; Sengers, J. V. Frame-invariant Fick diffusion matrices of multicomponent fluid mixtures. *Phys. Chem. Chem. Phys.* **2020**, *22*, 17597−17604, DOI: 10.1039/D0CP01110J.
(53) Wirnsberger, P.; Frenkel, D.; Dellago, C. An enhanced version of the heat exchange algorithm with excellent energy conservation properties. *J. Chem. Phys.* **2015**, *143*, 124104−124108.
(54) Liu, X.; Martín-Calvo, A.; McGarrity, E.; Schnell, S. K.; Calero, S.; Simon, J.-M.; Bedeaux, D.; Kjelstrup, S.; Bardow, A.; Vlugt, T. J. H. Fick Diffusion Coefficients in Ternary Liquid Systems from Equilibrium Molecular Dynamics Simulations. *Ind. Eng. Chem. Res.* **2012**, *51*, 10247−10258.
(55) Krishna, R.; Wesselingh, J. The Maxwell-Stefan approach to mass transfer. *Chem. Eng. Sci.* **1997**, *52*, 861−911.
(56) Maginn, E. J.; Messerly, R. A.; Carlson, D. J.; Roe, D. R.; Elliot, J. R. Best Practices for Computing Transport Properties 1. Self-Diffusivity and Viscosity from Equilibrium Molecular Dynamics. *J. Comput. Mol. Sci.* **2018**, *1*, No. 6324, DOI: 10.33011/livecoms.1.1.6324.
(57) Krishna, R.; van Baten, J. M. The Darken Relation for Multicomponent Diffusion in Liquid Mixtures of Linear Alkanes: An Investigation Using Molecular Dynamics (MD) Simulations. *Ind. Eng. Chem. Res.* **2005**, *44*, 6939−6947.
(58) Celebi, A. T.; Jamali, S. H.; Bardow, A.; Vlugt, T. J. H.; Moultos, O. A. Finite-size effects of diffusion coefficients computed from molecular dynamics: a review of what we have learned so far. *Mol. Simul.* **2021**, *47*, 831−845.
(59) Omrani, S.; Ghasemi, M.; Mahmoodpour, S.; Shafiei, A.; Rostami, B. Insights from molecular dynamics on CO_2 diffusion coefficient in saline water over a wide range of temperatures, pressures, and salinity: CO2 geological storage implications. *J. Mol. Liq.* **2022**, *345*, No. 117868, DOI: 10.1016/j.molliq.2021.117868.
(60) Liu, X.; Schnell, S. K.; Simon, J.-M.; Bedeaux, D.; Kjelstrup, S.; Bardow, A.; Vlugt, T. J. H. Fick Diffusion Coefficients of Liquid Mixtures Directly Obtained From Equilibrium Molecular Dynamics. *J. Phys. Chem. B* **2011**, *115*, 12921−12929.
(61) Dawass, N.; Krüger, P.; Schnell, S. K.; Simon, J.-M.; Vlugt, T. Kirkwood-Buff integrals from molecular simulation. *Fluid Phase Equilib.* **2019**, *486*, 21−36.
(62) Celebi, A. T.; Dawass, N.; Moultos, O. A.; Vlugt, T. J. H. How sensitive are physical properties of choline chloride-urea mixtures to composition changes: Molecular dynamics simulations and Kirkwood-Buff theory. *J. Chem. Phys.* **2021**, *154*, No. 184502.
(63) Ruckenstein, E.; Shulgin, I. Entrainer effect in supercritical mixtures. *Fluid Phase Equilib.* **2001**, *180*, 345−359.
(64) Krüger, P.; Schnell, S. K.; Bedeaux, D.; Kjelstrup, S.; Vlugt, T. J. H.; Simon, J.-M. Kirkwood-Buff Integrals for Finite Volumes. *J. Phys. Chem. Lett.* **2013**, *4*, 235−238.
(65) Ganguly, P.; van der Vegt, N. F. A. Convergence of Sampling Kirkwood-Buff Integrals of Aqueous Solutions with Molecular Dynamics Simulations. *J. Chem. Theory Comput.* **2013**, *9*, 1347−1355.
(66) Harris, J. G.; Yung, K. H. Carbon dioxide's liquid-vapor coexistence curve and critical properties as predicted by a simple molecular model. *J. Phys. Chem. A* **1995**, *99*, 12021−12024.
(67) Berendsen, H. J. C.; Grigera, J. R.; Straatsma, T. P. The missing term in effective pair potentials. *J. Phys. Chem. A* **1987**, *91*, 6269−6271.
(68) Dang, L. X. Development of nonadditive intermolecular potentials using molecular dynamics: Solvation of Li^+ and F^- ions in polarizable water. *J. Chem. Phys.* **1992**, *96*, 6970−6977.
(69) Smith, D. E.; Dang, L. X. Computer simulations of NaCl association in polarizable water. *J. Chem. Phys.* **1994**, *100*, 3757−3766.
(70) Dang, L. X. Mechanism and Thermodynamics of Ion Selectivity in Aqueous Solutions of 18-Crown-6 Ether: A Molecular Dynamics Study. *J. Am. Chem. Soc.* **1995**, *117*, 6954−6960, DOI: 10.1021/ja00131a018.
(71) Gaeta, F. S.; Perna, G.; Scala, G.; Bellucci, F. Nonisothermal matter transport in sodium chloride and potassium chloride aqueous solutions. 1. Homogeneous system (thermal diffusion). *J. Phys. Chem. A* **1982**, *86*, 2967−2974.
(72) Thompson, A. P.; Aktulga, H. M.; Berger, R.; Bolintineanu, D. S.; Brown, W. M.; Crozier, P. S.; in't Veld, P. J.; Kohlmeyer, A.; Moore, S. G.; Nguyen, T. D.; et al. LAMMPS - A flexible simulation tool for particle-based materials modeling at the atomic, meso, and continuum scales. *Comput. Phys. Commun.* **2022**, *271*, No. 108171, DOI: 10.1016/j.cpc.2021.108171.
(73) Andersen, H. C. Rattle: A "velocity" version of the shake algorithm for molecular dynamics calculations. *J. Comput. Phys.* **1983**, *52*, 24−34.
(74) Hockney, R. W.; Eastwood, J. W. *Computer Simulation Using Particles*, 1st ed.; IOP Publishing: London, 1988.
(75) Olsen, M. D.; Kontogeorgis, G. M.; Liang, X.; von Solms, N. Investigation of the performance of e-CPA for a wide range of properties for aqueous NaCl solutions. *Fluid Phase Equilib.* **2021**, *548*, No. 113167, DOI: 10.1016/j.fluid.2021.113167.
(76) Sun, L.; Kontogeorgis, G. M.; von Solms, N.; Liang, X. Modeling of Gas Solubility Using the Electrolyte Cubic Plus Association Equation of State. *Ind. Eng. Chem. Res.* **2019**, *58*, 17555−17567.
(77) Kontogeorgis, G. M.; Schlaikjer, A.; Olsen, M. D.; Maribo-Mogensen, B.; Thomsen, K.; von Solms, N.; Liang, X. A Review of Electrolyte Equations of State with Emphasis on Those Based on Cubic and Cubic-Plus-Association (CPA) Models. *Int. J. Thermophys.* **2022**, *43*, 54−68.
(78) Unver, A. A.; Himmelblau, D. M. Diffusion Coefficients of CO_2, C_2H_4, C_3H_6 and C_4H_8 in Water from 6 to 65 °C. *J. Chem. Eng. Data* **1964**, *9*, 428−431.
(79) Lu, W.; Guo, H.; Chou, I.; Burruss, R.; Li, L. Determination of diffusion coefficients of carbon dioxide in water between 268 and 473 K in a high-pressure capillary optical cell with in situ Raman spectroscopic measurements. *Geochim. Cosmochim. Acta* **2013**, *115*, 183−204.
(80) Colombani, J.; Dez, H.; Bert, J.; Dupuy-Philon, J. Hydrodynamic instabilities and Soret effect in an aqueous electrolyte. *Phys. Rev. E* **1998**, *58*, 3202−3208.
(81) Colombani, J.; Bert, J.; Dupuy-Philon, J. Thermal diffusion in (LiCl, RH_2O). *J. Chem. Phys.* **1999**, *110*, 8622−8627.
(82) Sell, A.; Fadaei, H.; Kim, M.; Sinton, D. Measurement of CO_2 Diffusivity for Carbon Sequestration: A Microfluidic Approach for Reservoir-Specific Analysis. *Environ. Sci. Technol.* **2013**, *47*, 71−78.
(83) Kraaijeveld, G.; Wesselingh, J. A. Negative Maxwell-Stefan diffusion coefficients. *Ind. Eng. Chem. Res.* **1993**, *32*, 738−742.
(84) Buchner, R.; Hefter, G. T.; May, P. M. Dielectric Relaxation of Aqueous NaCl Solutions. *J. Phys. Chem. A* **1999**, *103*, 1−9.

(85) Saravi, S. H.; Panagiotopoulos, A. Z. Activity coefficients of aqueous electrolytes from implicit-water molecular dynamics simulations. *J. Chem. Phys.* **2021**, *155*, No. 184501.

https://doi.org/10.1021/acssuschemeng.3c05269
ACS Sustainable Chem. Eng. 2023, 11, 17086−17097